fibers

MDPI

Article

Mitigating Out-of-Plane Fiber Waviness in AFP Laminates with Tow-Gaps via Selective Placement of Thermoplastic Veils

Ahmadreza Ravangard [1,*], Kuthan Celebi [2], Sergii G. Kravchenko [2] and Oleksandr G. Kravchenko [1,*]

[1] Department of Mechanical and Aerospace Engineering, Old Dominion University, Norfolk, VA 23529, USA
[2] Department of Materials Engineering, The University of British Columbia, Vancouver, BC V6T 1Z4, Canada; kuthan.celebi@ubc.ca (K.C.); sergey.kravchenko@ubc.ca (S.G.K.)
* Correspondence: arava001@odu.edu (A.R.); okravche@odu.edu (O.G.K.)

Highlights

What are the main findings?

- Selective placement of thermoplastic veils within AFP tow-gaps reduces ply sinking, surface waviness, and fiber misalignment.
- Veils transform resin-rich regions into reinforced networks, improving laminate mechanical and morphological uniformity.
- Tensile testing and progressive failure simulations demonstrate that veil placement restores stiffness and induces changes in failure behavior.

What is the implication of the main findings?

- Controlling morphology through targeted veil placement enhances composite reliability without weight increase.
- The method offers an approach for mitigating AFP tow gap induced defects.

Abstract

Fiber tow-gaps and overlaps formed during the Automated Fiber Placement (AFP) process pose a significant challenge by introducing non-uniform composite morphologies, often characterized by resin-rich regions and fiber waviness. These defects occur as deposited fibers sink into the gap regions during consolidation, with gap geometry determined during path planning. Such morphological inconsistencies can compromise structural reliability by initiating premature failure, particularly through localized out-of-plane waviness and resin accumulation. This study investigates the integration of high melting temperature thermoplastic veils, specifically polyetherimide (PEI), into fiber tow-gaps as a method to prevent ply sinking and reduce fiber waviness on both internal and external surfaces of the laminate. The PEI veils also serve to reinforce resin-rich regions by forming an interpenetrated network of high fracture toughness material within the brittle epoxy matrix. Tensile tests conducted on cross-ply laminates containing staggered gaps demonstrated that the inclusion of PEI veils modified the failure mode. The results suggest that the selective placement of thermoplastic veils within tow-gaps during AFP offers a viable strategy to mitigate manufacturing-induced non-uniform morphologies.

Keywords: automated fiber placement; fiber tow-gaps; out-of-plane fiber waviness; resin-rich regions; thermoplastic veils

check for updates

Academic Editor: John W. Gillespie

Received: 11 August 2025
Revised: 26 September 2025
Accepted: 17 October 2025
Published: 24 October 2025

Citation: Ravangard, A.; Celebi, K.; Kravchenko, S.G.; Kravchenko, O.G. Mitigating Out-of-Plane Fiber Waviness in AFP Laminates with Tow-Gaps via Selective Placement of Thermoplastic Veils. *Fibers* **2025**, *13*, 145. https://doi.org/10.3390/fib13110145

Copyright: © 2025 by the authors. Licensee MDPI, Basel, Switzerland. This article is an open access article distributed under the terms and conditions of the Creative Commons Attribution (CC BY) license (https://creativecommons.org/licenses/by/4.0/).

1. Introduction

Automated Fiber Placement (AFP) is an advanced manufacturing process for primary composite structures, particularly in aerospace [1–3]. AFP offers an industrial advantage of full automation: computer-controlled heads can lay multiple tows in each course with repeatable accuracy, drastically reducing labor, cycle times, and human error. This automation enables the fabrication of large, contoured structures such as wing skins, fuselage barrels, and cryogenic tanks that would be impractical or cost-prohibitive with hand lay-up or conventional tape-lay methods, while still accommodating complex variable-stiffness layups and in situ quality monitoring [4]. AFP introduces features like fiber tow-gaps and overlaps during the fabrication, governed by processing parameters and fiber layup trajectories [5,6]. These features have a propensity to become defects in the cured composite and can be seen as morphological inconsistencies in the laminate, including fiber waviness, resin-rich regions, and ply thickness variations, which compromise mechanical performance [7–10]. Resin flow during compaction, influenced by anisotropic viscosity, leads to resin-rich zones that act as stress concentrators [11–13]. In multidirectional composite laminates, resin pockets reduce stiffness minimally but can lower failure strain by up to 20% [14]. Key contributors to resin-rich regions include stacking sequences and manufacturing parameters, which influence resin flow dynamics. Resin-rich regions complicate the mechanical behavior of composites making it less predictable and can be linked to other morphological irregularities [15,16]. Furthermore, unevenness in composite surfaces due to the presence of the fiber tow-gaps can affect dimensional tolerance in the primary structures needed for aerodynamic and assembly considerations.

Defects in cured AFP composites can originate from misaligned tows, as well as steering, which create gaps and overlaps that significantly affect composite mechanical behavior. Static tension, compression, and fatigue tests reveal that compressive strength reductions can be up to 25%, compared to 10% for tensile strength. Defect configurations, like wider defects in 45° orientations, may increase compressive strength but reduce tensile performance [17]. The defect impact on open-hole compression (OHC) strength depends on location, with effects ranging from positive to negative. For instance, 90° centered gaps reduce OHC strength by 7.1%, and additional shifted gaps exacerbate reductions to 13% [18]. Fiber waviness further impacts properties, initiating premature failure under static and cyclic loads [10,19–21]. Increased fiber waviness angles decrease failure stress beyond 20% [22]. Fatigue performance is also affected, with fiber waviness contributing to stiffness reduction and load redistribution [23]. As seen from this discussion, while tow-gaps may not be avoidable, strategies on how to minimize their effects on the behavior of composite laminates need to be explored. One possible solution can be the selective placement of low areal density non-woven thermoplastic veils, which can suppress ply sinking without contributing significant parasitic weight within carbon-fiber-reinforced polymer (CFRP) epoxy matrices. These veils have demonstrated the ability to improve damage tolerance by enhancing interlaminar fracture toughness through bridging of delamination cracks [24–27]. While the implementation of veil placement during AFP is beyond the scope of this study, the observed benefits in controlling morphology around tow-gaps highlight a promising direction for future research on AFP-integrated veil placement. The delivery of such veils can be potentially automated using one of the available spools in the AFP head [28].

To explore this idea, this study investigates the mechanics of compaction and the resulting influence on the mechanical behavior of benchmark composite laminates with rectangular tow-gaps. The selective incorporation of polyetherimide (PEI) veils within the benchmark configuration was used to explore the effect on composite morphology around fiber tow-gaps by preventing ply sinking, which helps mitigate formation of out-of-plane fiber waviness. The presented approach was used as a testbed to explore the

effects of the potential placement of thermoplastic veils into the region of severe staggered tow-gaps with simplified geometry. The paper is organized as follows. Section 2 details the experimental methods including sample fabrication with controlled gap staggering and incorporation of veils. Characterization techniques, including optical microscopy, surface profilometry, micro-computed tomography (micro-CT), and tensile testing with full-field Digital Image Correlation (DIC), are described in Section 2. Section 3 presents the modeling approach used to simulate the compaction process and evaluate the structural response using progressive failure analysis. Section 4 presents the key findings, while Section 5 summarizes conclusions and outlines future work. The incorporation of PEI veils allowed for reductions in fiber waviness, which led to a moderate reduction in the stress knockdown seen due to ply sinking. DIC analysis revealed that the presence of veils had an influence on the damage process and, therefore, had an implication on the overall composite behavior. In conclusion, the present work indicates a potential for adopting thermoplastic veils to ensure greater control over the resulting AFP composite morphology. Furthermore, it introduces a benchmark problem for analyzing AFP-induced waviness and resin-rich regions in relation to selective veil placement, which has not been addressed in previous studies on veil-toughening or AFP defect studies [25,26].

2. Experimentation

2.1. Materials and Sample Fabrication

This study employed the HexPly® IM7/8552 carbon-fiber composite prepreg from Hexcel Corporation (Stamford, CT, USA), designed for AFP due to its minimal tack properties [29]. To investigate the influence of staggered-gap configurations on fiber morphology, composite laminates were fabricated using a [0°, 90°, 0°, 90°, 0°, 90°, 0°] stacking sequence. This anisotropic stacking sequence was chosen to test the effect of 90° gaps (meaning orientation in y-direction) on the strength knockdown in the x- and y-direction. It is important to note that during tensile testing in the x-direction, the 0° plies are the main load-carrying plies. In contrast, during y-direction testing, the 90° plies carry most of the load, and the gaps do not have the same effect. Samples were fabricated manually by placing 6.25 mm (0.25″) wide carbon-fiber tows and gaps following the configuration in Figure 1. A hand roller was employed to provide uniform compaction pressure across each ply. Panels were fabricated as a benchmark problem to study the compaction response of laminates with tow-gap features. The manual layup with roller compaction followed by an autoclave cure was adequate to reproduce the compaction and resin-flow mechanisms of AFP composites. This approach provided flexibility to define gap configurations, enabling systematic evaluation of veil effects within a reproducible benchmark framework. PEI veils were incorporated within and around the regions of tow-gaps to investigate the effect on preventing ply sinking. Figure 2 illustrates the stacking configuration and integration of thermoplastic veils within a staggered-gap composite laminate. The red layers represented thermoplastic veils positioned inside of the gap regions and interlaminar regions around the tow-gap, extending 12.7 mm past the gap. The PEI veil used in the VEIL samples had a nominal areal weight of 10 g/m^2, corresponding to a thickness of approximately 0.10 mm or about 75% as thick as a single ply of the IM7/8552 carbon-fiber composite (≈0.135 mm). To maximize veil effectiveness, two strips of thermoplastic veil were inserted into each tow-gap region, ensuring the gap volume remained fully occupied during consolidation. This configuration aimed at preventing the upper plies from sinking into the gap. Additionally, a single strip of veil was placed at interlaminar locations adjacent to the gaps to toughen the interlaminar region and improve load transfer around tow-gap. Therefore, the veil provided a porous scaffold that supported overlying fibers and resisted ply sinking, while supporting a more uniform compaction.

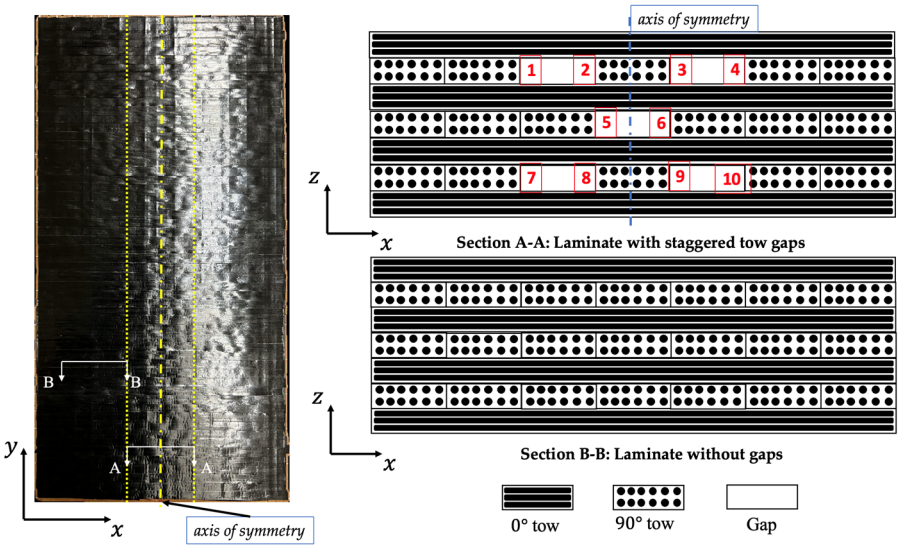

Figure 1. Composite laminate with staggered tow-gaps and layup cross-section schematics for sections A-A and B-B. The yellow dashed line indicates the axis of symmetry, while the yellow dotted lines outline the region containing tow gaps. The red boxes (1–10) mark the tow gap regions sides, and the red color represents the veil layer in the laminate.

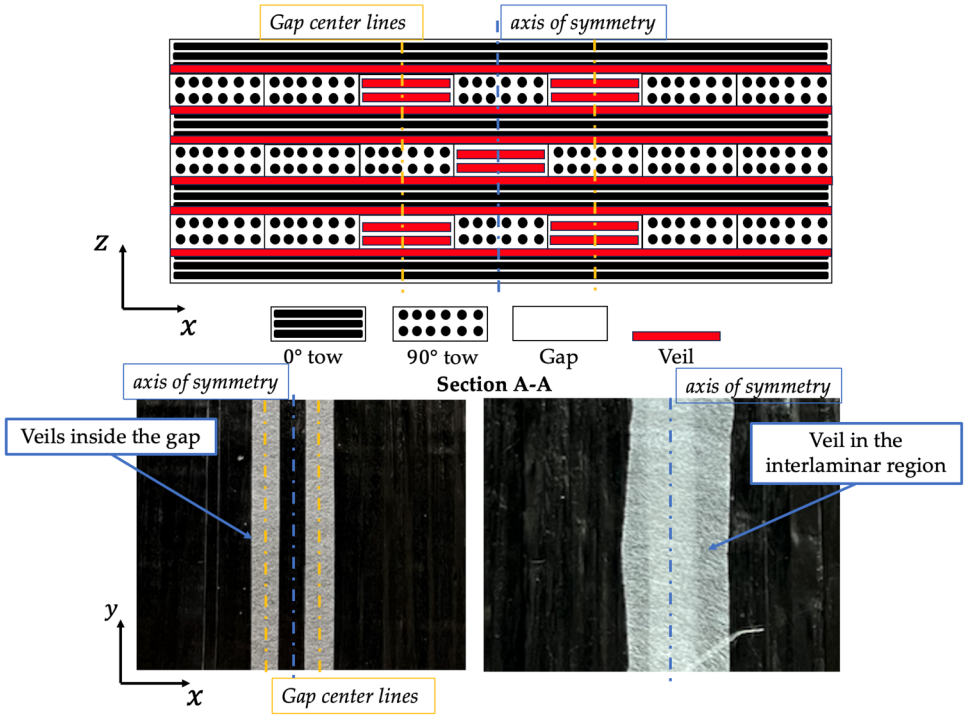

Figure 2. Schematic and photos showing the placement of thermoplastic veils within fiber tow-gaps and interlaminar regions in a cross-ply composite laminate with staggered-gap configuration.

The curing process for HexPly® 8552 composite laminates followed the manufacturer's cure cycle (Hexcel Corporation, Stamford, CT, USA) [30]. From the cured panels, various samples were extracted using a water jet, including pristine samples (without gaps), samples with gaps, and samples with PEI veils inserted into the gaps. The samples were categorized based on their loading directions. Pristine samples were tested along the x- and y-axes, labeled as PR_x and PR_y, respectively. Similarly, samples with gaps and veils were tested in two orientations, labeled GAP_x, GAP_y, $VEIL_x$, and $VEIL_y$. GAP_x and $VEIL_x$ samples were loaded perpendicular to the gap direction, while GAP_y and $VEIL_y$

samples were loaded parallel to the gap direction. Some samples were designated for microstructural analysis, to evaluate non-uniform morphology around the gap region. Figure 3 illustrates the extracted samples and their loading orientations. The specimen loaded in the x-direction was designed with dimensions of 177.8 mm in length and 25.4 mm in width, with 25.4 mm tabs at both ends to facilitate tensile testing. The specimen loaded in the y-direction had a length of 177.8 mm and a width of 44.5 mm, with the tabbing width adjusted to accommodate the increased specimen width.

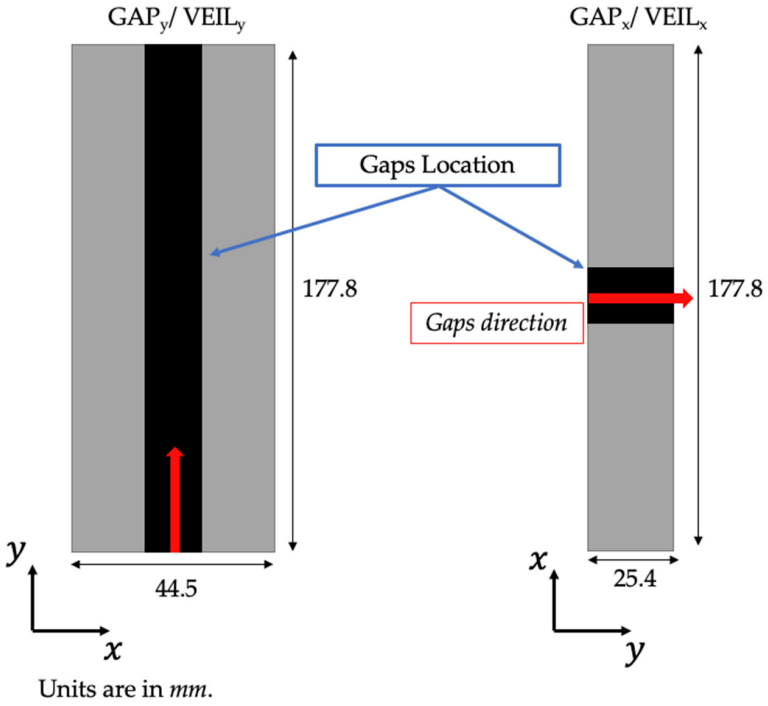

Figure 3. Schematic of different extracted samples from composite panel.

2.2. Micro-Computed Tomography

Internal morphology features and void distributions were examined with micro-CT. Scans were carried out on a laboratory system under multiple resolutions and scan modes (see Figure 4). Scans were performed using the Rigaku CT Lab HX130, a high-resolution benchtop X-ray CT scanner designed for non-destructive 3D imaging of materials. Voxel sizes ranged from 10.1 µm to 25.2 µm, and total scan times varied from 17 min to more than 4 h, depending on the chosen projection settings and field of view.

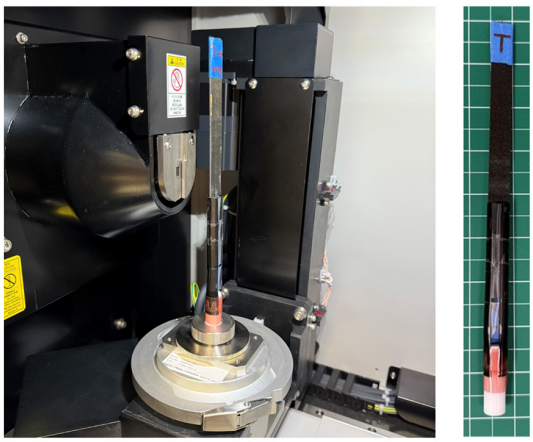

Figure 4. Micro-CT scanning setup (**left**) and prepared composite specimen mounted in a sample holder (**right**) for internal structural analysis and high-resolution imaging.

2.3. Mechanical Testing and Digital Image Correlation

Quasi-static tensile tests were performed on an MTS™ (Material Testing Systems, MTS Systems Corporation, Eden Prairie, MI, USA) universal testing machine at a constant crosshead speed of 3 $mm \cdot min^{-1}$. Load–displacement data were recorded in real time using MTS TestSuite™ v4.10 software. Full-field strain was captured with a two-camera DIC system. Images were acquired with GOM®Snap v2.0.1 and processed in GOM®Correlate v2.0.1.

2.4. Microscopy Analysis

High-resolution optical micrographs were obtained with a Leica DM6 M microscope (Leica Microsystems GmbH, Wetzlar, Germany), while low-magnification overview images were taken on a Leica S9 stereomicroscope. Specimens were wet-ground sequentially with 120, 320, and 600 grit silicon-carbide papers, then polished with 6 µm and 1 µm diamond suspensions followed by a final 0.04 µm colloidal-silica polish to achieve a mirror-like finish. All samples were vacuum-mounted in low-shrinkage resin as a part of sample preparation.

2.5. Surface Profilometry

All profilometry data were acquired using a Leica DCM8 optical profiler (Leica Microsystems GmbH, Wetzlar, Germany), with a lateral resolution of approximately 2 µm (resulting in over 5000 measurement points along the 10 mm scan), and processed using Leica LAS X (office widefield) and Leica Map360 software. The system was calibrated using National Institute of Standards and Technology (NIST)-traceable step-height standards of 50 µm, 100 µm, and 200 µm; this procedure verified vertical accuracy within $\pm$ 0.5 µm ($\leq$0.25% error) and demonstrated reproducibility below 0.2 µm across the full measurement range.

3. Modeling

3.1. Process Modeling Approach

A 3D model with explicit staggered tow-gap geometry was generated and meshed with 1800 8-node thermally coupled brick elements (C3D8Ts) (Figure 5). Mesh density was refined in the gap region and coarsened elsewhere. Orthotropic, cure-dependent behavior was implemented through user subroutines (VUMAT/VUMATHT) with state variables that included degree of cure, resin viscosity, effective ply stiffness, thermal properties, and fiber orientation [11]. The simulation was performed in Abaqus/Explicit with a 5400 s dynamic temperature–displacement step, stabilized with mass scaling and bulk viscosity. Autoclave processing was modeled on the top side of the laminate by ramping up to the uniform pressure of 0.7 MPa, while temperature was applied through the convection boundary condition following the cure profile. The details on the model can be found in [11]. The bottom tool side restricted the displacement in the vertical direction $u_z = 0$ (in-plane free) with thermal contact conductance to the tool. The sides had traction-free and adiabatic conditions. The cure followed the manufacturer's recommended cure cycle for HexPly IM7/8552 (Hexcel Corporation, Stamford, CT, USA) [30].

A previously developed fully coupled thermo-chemo-mechanical framework was implemented to simulate the compaction of uncured AFP laminates [11]. This enabled simulation of tow-gap deformation during manufacturing and use of the predicted morphology for subsequent Progressive Failure Analysis (PFA). The prepreg was modeled as a transversely isotropic, hyper-viscoelastic medium whose resin viscosity evolved with temperature and degree of cure, using a modified autocatalytic kinetics law to capture resin stiffening during the early, highly deformable stage [11]. More details on this approach can be found in the previously published work [11]. The purpose of this analysis in this study was to use the simulated compacted geometry for structural analysis. Once compaction simulation was completed, the fully deformed mesh (including ply waviness, local

thickness variations, and filled tow-gaps) was extracted directly from the Abaqus database and exported for PFA input (Figure 6). In the follow-on analysis, this process-driven morphology underpinned the high-fidelity PFA modeling.

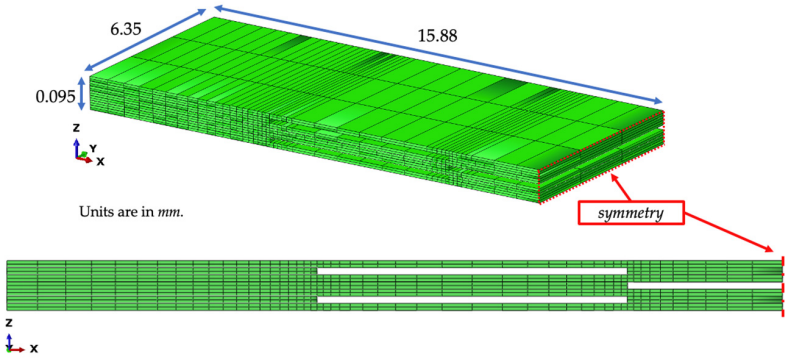

Figure 5. Mesh of staggered tow-gap cube with 1800 C3D8T elements and symmetry plane.

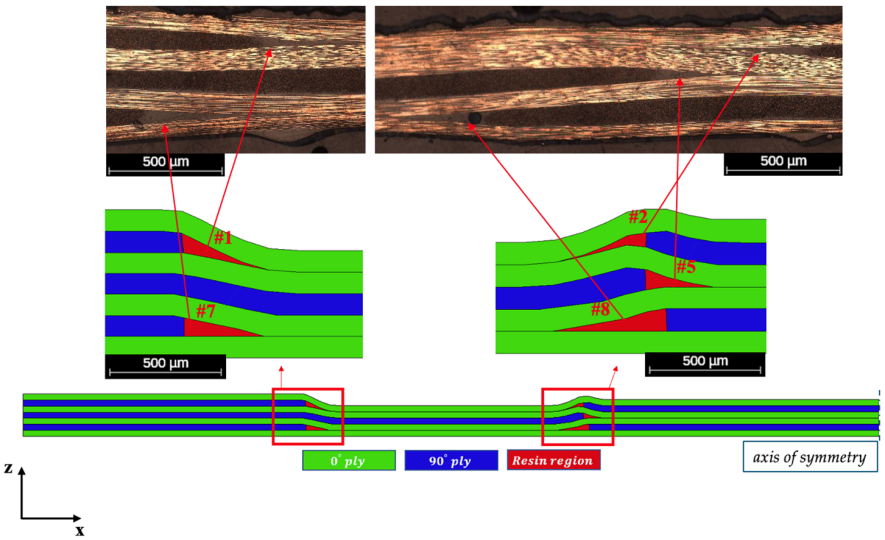

Figure 6. Compaction model geometry extracted from compaction simulation (**bottom**) alongside corresponding optical micrographs (**top**), demonstrating close agreement between predicted ply deformation and resin-rich pocket formation and actual coupon cross-sections. The numbers indicate the resin-reach regions corresponding to the gap-closure side numbers shown in Figure 1.

By integrating a fully coupled thermo-chemo-mechanical compaction simulation with PFA, this work enabled evaluation of the role of fiber waviness developed due to gap placement in the resulting failure propagation.

3.2. PFA Modeling Approach

For the failure analysis of the compaction-deformed morphology, NASA's CompDam framework was adopted due to its comprehensive representation of ply-level damage mechanisms [31,32]. CompDam uses deformation-gradient decomposition (DGD) to embed cohesive planes within each ply, enabling explicit modeling of intralaminar matrix cracks without refining the mesh around every crack tip [33]. Delamination was modeled through cohesive-zone elements between plies, and fiber tensile failure was predicted by local stress criteria. By applying DGD directly to the deformed mesh from the compaction simulation, manufacturing-induced features, such as ply waviness, thickness variation, and resin-rich pockets, were integrated within the PFA modeling. This integrated approach provided high-fidelity predictions of strength reductions and damage progression. The properties used for PFA modeling are presented in Tables A1 and A2 (in the Appendix A).

Extraction of the deformed mesh from Abaqus allowed direct visualization of manufacturing-driven defects, bridging the gap between AFP process parameters and resulting laminate morphology. Applying PFA via the DGD framework on these process-driven meshes captured the evolution of intralaminar cracking, cohesive-zone damage, and delamination, as discussed in the following sections.

4. Results

4.1. Surface Profilometry

Profilometry scans started 10.58 mm from the outer gap centerline and spanned inward to the gap centerline. The height map of the region over the staggered gaps (Figure 7a,b, labeled Staggered gaps: no veil and Staggered gaps: with veil) revealed surface waviness, evidenced by transitioning from a low to high depth across a 10.58 mm profile scan taken over the central portion of the gap region. The change in depth in the GAP sample was about 0.47 mm, whereas samples with the PEI veils had a significantly reduced change in depth of about 0.23 mm (Figure 7c). These variations in the local depth of composite were attributable to gaps in the fiber tows. Compaction of the AFP composite during manufacturing created a non-uniform, uneven surface in primary structures, which is undesirable for design. In the GAP sample, the depth profile was more irregular (showing changes of up to 0.43 mm before gradually decreasing), pointing to significant surface unevenness and ply waviness arising from ply sinking, which was typically associated with other defects in the cured morphology, such as triangular-shaped resin-rich regions and fiber out-of-plane waviness. The height map of the VEIL sample exhibited a smoother and more confined range of height variations.

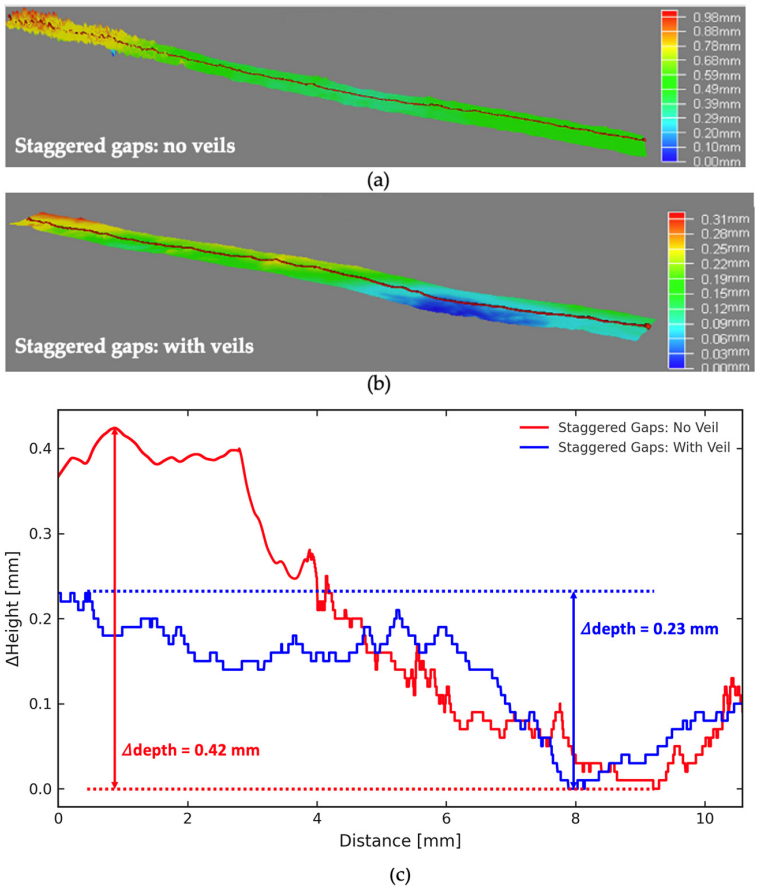

Figure 7. Surface height maps of a tow-gap region (**a**) without and (**b**) with PEI veils, and (**c**) corresponding line profiles showing reduced peak-to-valley height.

4.2. Microstructural Observations

As seen from the micrographs, the veils acted as a scaffold inside of the gap, while providing sufficient permeability for the resin to fill the voids inside of the porous veil. Figure 8 presents high-resolution optical micrographs of composite laminates fabricated without thermoplastic veils, revealing significant resin-rich regions. These resin-rich regions, formed from the original tow-gaps, introduced out-of-plane ply waviness (most notably in the 0° layers) that also resulted in ply and laminate thickness variation across the cross-section. At the corner of each original tow-gap (left and right) placed in the laminate, the resin-rich region was formed approximately 250–400 μm in length. Since there were five tow-gaps, this produced a total of ten resin-rich regions (see Figure 1), arranged symmetrically with respect to the axis of symmetry for the initial gap configuration. As a result, the fiber out-of-plane waviness in the neighboring plies, directly above and below the gap region, was formed. Figure 8 shows the overall view on the cross-section, while the zoomed-in view provides the details of the resin-rich regions to the left of the axis of symmetry. These resin pockets appeared as translucent or light-colored bands between displaced fibers that were pushed into the gap region and adjacent plies. Some 90° fiber tows were "squeezed" into the gaps (indicating an imbalance in compaction pressure) but failed to fully bridge the void, leaving large resin-rich zones unreinforced.

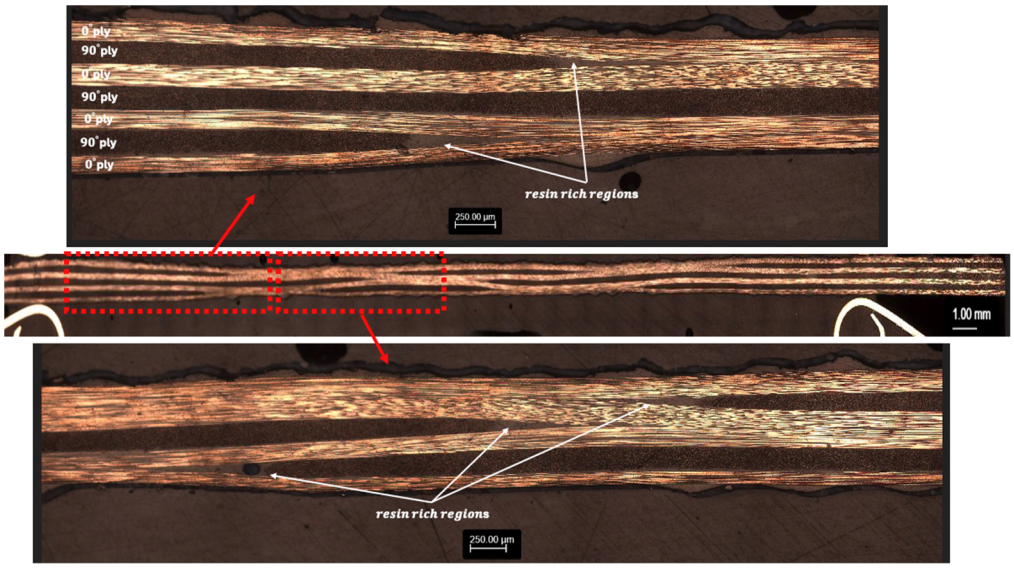

Figure 8. Micrographs illustrating the cross-sectional morphology of the gap region without veils.

Figure 9 depicts micrographs of samples in which thermoplastic veils had been placed inside the tow-gaps and within the interlaminar region. Here, the same region representing the initial staggered-gap pattern exhibited a more uniform thickness profile: resin-rich packets were reduced to below 50 μm (often barely detectable in a cross-section), and the ply alignment remained consistent through the entire thickness. The veil material supported the 0° tows above it, preventing their sinking inside of the gap. As a result, the cured laminate did not show as pronounced out-of-plane fiber waviness that was observed in GAP sample, thus promoting a more uniform ply morphology and a reduced resin-rich region. Since veils are known for their toughening effect, this can also provide the potential benefit of reinforcing the resin-rich region. However, some of the veil appeared to be located under the 90° ply (Figure 9), even though the initial placement of the veil was side-by-side with the 90° ply. This, along with the shifted locations of the resin-rich triangular regions (Figure 7), indicates the shifting of the 90° ply, driven by the squeeze flow,

which contributes to some waviness in the 0° plies. To quantify the apparent out-of-plane waviness in the un-veiled (GAP) and veiled samples, micro-CT analysis was performed.

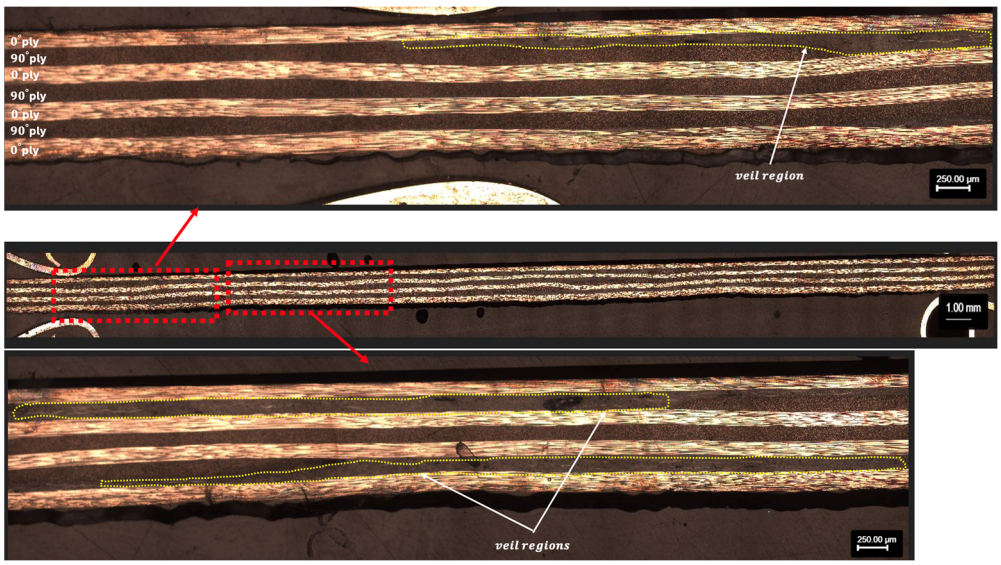

Figure 9. Micrographs illustrating the cross-sectional morphology of the gap region with a thermoplastic veil.

4.3. Internal Morphology Characterization via Micro-CT

Three tow-gap samples were inspected using micro-CT data. Two samples, one with and one without a PEI veil, were both scanned at 10 and 25 µm resolutions. The lower resolution scans captured a larger field of view, comprising a higher number of gap regions, while the higher resolution scans enabled a more detailed evaluation of morphology and fiber waviness. A third sample without a PEI veil was also scanned at a 3 µm resolution to quantitatively analyze fiber orientations and resin-rich regions. Figure 10 presents high-resolution micro-CT cross-sections of composite laminates, comparing regions "without veil" (left column) to "with veil" (right column) in both the gap zone (top row) and the interlaminar zone (bottom row). In the gap region without veil, the grayscale contrast was quite uniform, with a broad midtone band stretching across most of the field. This uniformity corresponded to a gap where very few high-attenuation (i.e., carbon fiber) structures are visible. In other words, the tow-gap had collapsed into a resin-dominated channel, and the lack of bright, fibrous features indicated that the 90° fibers had not bridged the void. By contrast, the region of gap with veil revealed a network of fine, interwoven veil that was infused with resin. Resin had percolated through the veil (dark resin-filled areas are interspersed, rather than monolithic, with bright PEI fibers) indicating that the fiber and resin phases formed an interpenetrated network. This fiber–veil scaffold effectively preserved some of the original through-thickness integrity, preventing a large resin channel from forming.

Looking at the interlaminar region with no veil, the matrix-dominated zone was seen, while with the addition of a veil, the interpenetrated PEI–resin network with minimal porosity could be observed. Across both gap and interlaminar locations, the micro-CT images made it clear that the thermoplastic veil altered the structure of the interlaminar region; the veil similarly prevented the formation of a homogeneous resin layer, instead introducing a finely interwoven veil structure that enhanced through-thickness fiber connectivity.

Figure 11 presents two complementary views of the out-of-plane fiber orientation in the un-veiled laminate. In Figure 11a, a grayscale CT scan is shown at Section A-A, with four tow-gaps labeled 1, 5, 7, and 8 (see Figure 1). At each gap edge, a green wedge and red reference lines marked the local fiber axis, and the out-of-plane angles were measured

as $\varphi_1 = 6.65°$, $\varphi_7 = 5.20°$, $\varphi_5 = 8.90°$, and $\varphi_8 = 7.14°$. The presence of ply waviness in the un-veiled sample could be inferred from the CT scan results. Discrete measurements of fiber orientation adjacent to each tow-gap revealed out-of-plane angles ranging from 5.20° to 8.90°, indicating that the fibers deviated from the intended planar alignment. This pattern was further supported by the heatmap (Figure 11b), where narrow bands of high misalignment (up to 10°) were observed. These bands were sharply localized, with the fiber angle rapidly returning to near zero just a few hundred microns away from each gap. The combination of periodic fiber tilting at the gap edges and the recurring high-angle regions in the heatmap confirmed the presence of ply waviness.

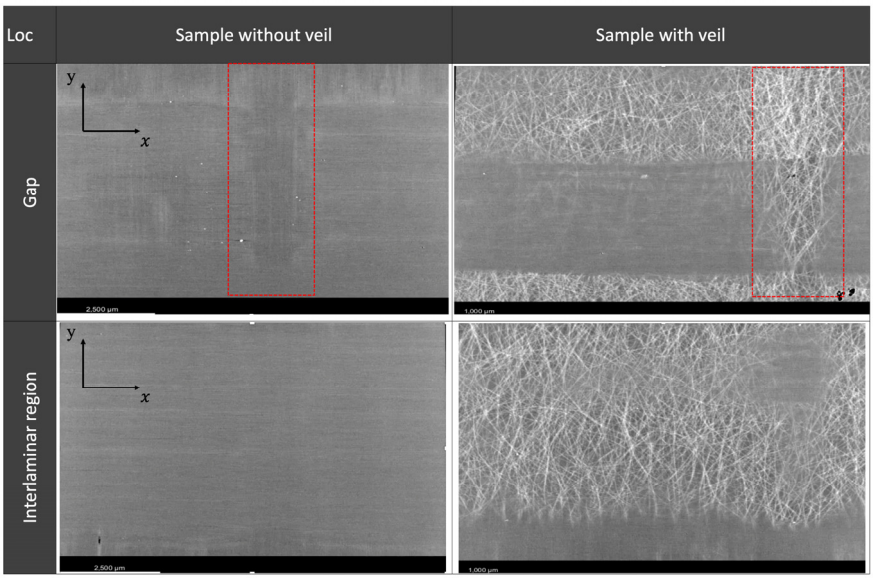

Figure 10. Micro-CT images comparing microstructures of samples without (**left**) and with (**right**) thermoplastic veils in the gap (**top**) and interlaminar (**bottom**) regions. Red dashed boxes highlight the gap zones. The red boxes indicate the locations of visible surface dents, which stem from the presence of the gap that transforms into an indentation after the compaction process.

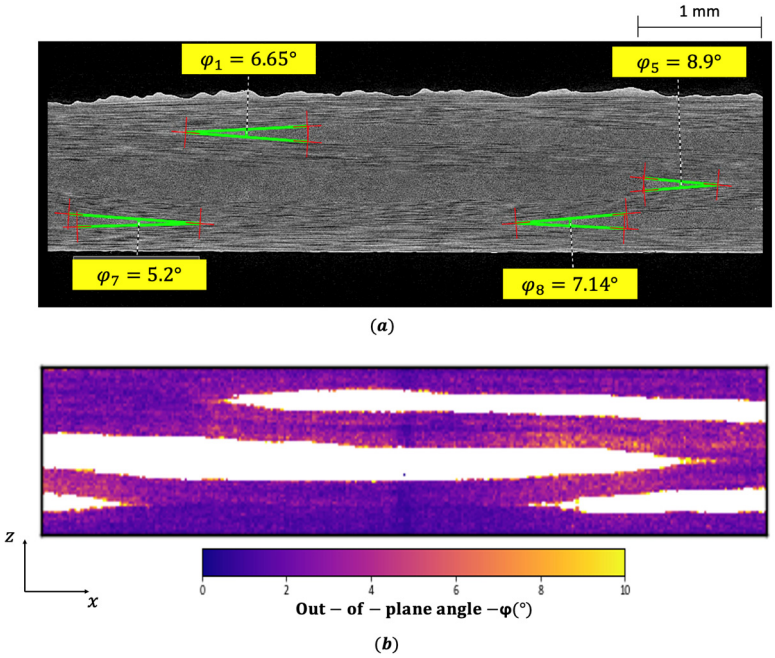

Figure 11. (**a**) CT scan showing out-of-plane fiber angles adjacent to tow-gaps; (**b**) heatmap of φ(x,z) reveals localized ply waviness up to 8.9° at gap edges.

In Figure 12, out-of-plane fiber misalignment angles (φ) at the corners of resin-rich regions were compared for samples with and without the PEI thermoplastic veil. In the un-veiled sample, measured φ angles at Gaps 2, 3, 4, 5, 6, 8, and 9 ranged from 4.1° to 9.1°, with an average value of 6.1°. The highest values were observed at Gaps 3 (8.2°), 4 (7.7°), and 6 (9.1°), indicating localized ply waviness at these regions. In contrast, the veiled sample showed much smaller and more uniform φ values ranging from 3.54° to 5.86°, with an average of 4.5°. Notably, the highest angle in the veiled sample (5.86° at Gap 4) was still significantly lower than the maximum in the un-veiled sample. The addition of the PEI veil led to a 54% reduction in the maximum out-of-plane angle (from 9.1° to 5.86°) and a 36% reduction in the average misalignment (from 6.1° to 4.5°). While only section-cut views were shown, the angle was found to be consistent throughout the scanned region, further confirmed that the observed improvements were representative of the entire laminate.

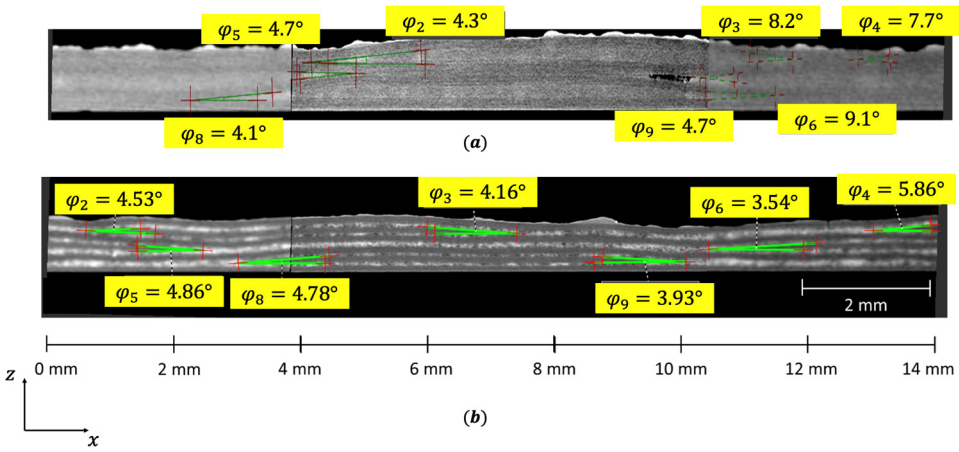

Figure 12. (**a**) CT scan of sample without PEI veil; (**b**) CT scan of veiled sample.

4.4. Tensile Testing

The present cross-ply laminate contained four 0° plies (aligned in the *x*-axis) and three 90° plies (aligned in the *y*-axis). Therefore, the 0° layers were the primary load-carrying plies in x-direction tests, whereas the 90° layers dominated in y-direction. As a result of the selected stacking sequence, which had four 0° and three 90° plies, pristine composite laminate demonstrated higher average strength in the x-direction (1480 MPa) compared to the y-direction (1180 MPa). Under tensile loading, pristine laminates (PRs_x) exhibited a peak stress at a failure strain of 0.015 mm/mm and an initial stiffness of ~81 GPa (Figure 13a, black curve). As seen previously, the introduction of a tow-gap (GAP_x, red curve) created a 250–400 µm resin-rich pocket that functioned as a localized stress concentrator, reducing peak strength to ~1300 MPa and decreasing failure strain to 0.013 mm/mm. When the gap was filled with a thermoplastic veil ($VEIL_x$, green curve), the strength recovered to 1476 MPa, stiffness increased to 100 GPa, and failure strain was marginally reduced to 0.0122 mm/mm.

Figure 13b shows pristine specimen (PR_y) tensile behavior with strength of 1190 MPa at 0.016 mm/mm with a stiffness of ~75 GPa. Since the gap was oriented aligned with the load (GAP_y) for this loading case, the sinking was still prevented in 0° plies, which were not load bearing for the y-direction. More importantly, the omission of five 90° tows reduced the strength to ~700 MPa and caused the stiffness to fall to ~60 GPa. Therefore, the effect of veils could not compensate for the missing fiber tow, and thus no noticeable difference between GAP_y and $VEIL_y$ was found. Because the veil is a low-stiffness thermoplastic that reduces waviness in non-load bearing 0° plies in the y-direction, it offered little strength recovery. The effect of the veil was, however, seen in the resulting variation in strength, and the damage propagation, which is discussed in the following section.

Figure 14 presents box-and-whisker plots of maximum stress across all specimens, corroborating these trends quantitatively. Under x-loading, the median strength decreased from 1480 MPa (PR_x) to 1430 MPa (GAP_x) before rising to 1500 MPa ($VEIL_x$), with reduced variability (COVs of 0.01, 0.101, and 0.087 for PR_x, GAP_x, and $VEIL_x$, respectively). A two-sample *t*-test showed that although the veil restored median strength to near-pristine levels and lowered scatter by roughly 14%, the difference in mean strength between GAP_x and $VEIL_x$ was not statistically significant ($p \approx 0.23$, $\alpha = 0.05$). Under y-loading, medians fell from 1150 MPa (PR_y) to 730 MPa (GAP_y) and to 700 MPa ($VEIL_y$), with notable scatter in GAP_y (COV = 0.114) compared to PR_y (COV = 0.04) and $VEIL_y$ (COV = 0.075). Similarly, no significant difference in mean strength was found between GAP_y and $VEIL_y$ ($p \approx 0.16$), indicating that the veil mainly reduces variability rather than increasing strength when the 90° plies carry the load. These data affirmed that thermoplastic veils could compensate for some of the strength knockdown by reducing waviness in the load-bearing plies. While the increase in mean strength was not statistically significant at the 5% level, the veil clearly lowered scatter, and as a result the COV for y-strength was reduced once veils were incorporated. This in itself has an important effect for the A-basis design of primary structures: tighter distributions of the mechanical properties allow for greater control of the design allowable [34].

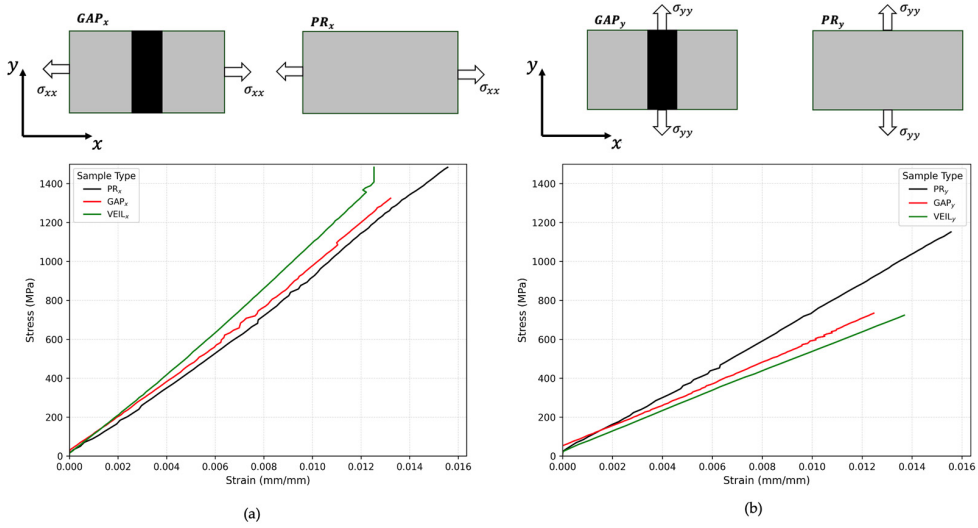

Figure 13. Stress versus strain response for the samples under tension: (**a**) along the x-direction (**b**) y-direction.

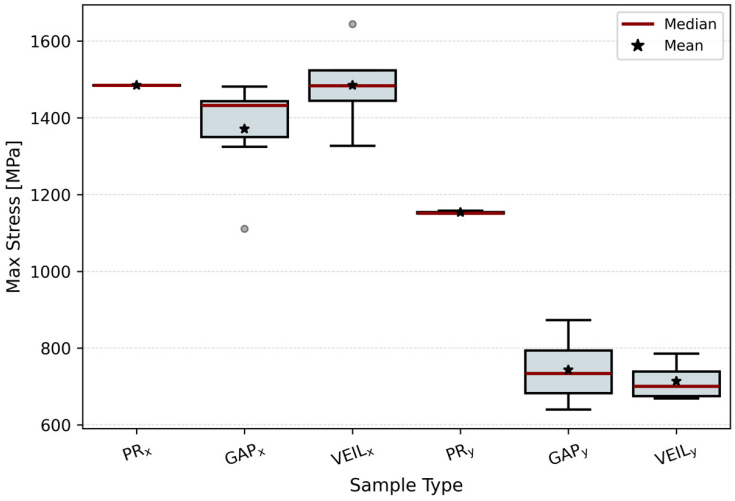

Figure 14. Strength distribution of composite samples: pristine (PR), with gaps (GAP), and with veils (VEIL) in x- and y-directions.

4.5. Strain Distribution Analysis Using DIC

The DIC strain maps in Figures 15 and 16 illustrate how morphological changes (GAP vs. VEIL samples) translated into distinct strain signatures under loading in both x- and y-direction. Under x-direction (Figure 15), the pristine sample (PR_x) displayed a nearly uniform ε_{xx} field on the surface, with strain values predominantly in the 1.2–1.6% range, with some spatially distributed regions of 2% strain. When a tow-gap was introduced (GAP_x), instead of uniform strain field, significant strain concentration was observed in the locations of fiber waviness, with peak ε_{xx} values reaching 1.8–2.0%. The high-strain band spanned across the sample with a spacing of 8 mm, which indicates the impression in the top surface because of staggered gaps and resulting ply sinking (Figure 15). The unreinforced resin pockets at the corner of the original gaps and resulting ply waviness introduced geometric nonlinearity and acted as a local stress concentrator—this behavior is later illustrated with the result of PFA using FE simulation of the gap sample. The veil-reinforced sample ($VEIL_x$) showed a smoother ε_{xx} distribution compared with GAP_x: most of the strain field remained within 0.8–1.2% (green to light yellow). Like the GAP_x sample, two strain streaks were observed; however, in the $VEIL_x$ sample, the spacing between the strain bands was markedly reduced from 12 mm in GAP_x to 4 mm in $VEIL_x$.

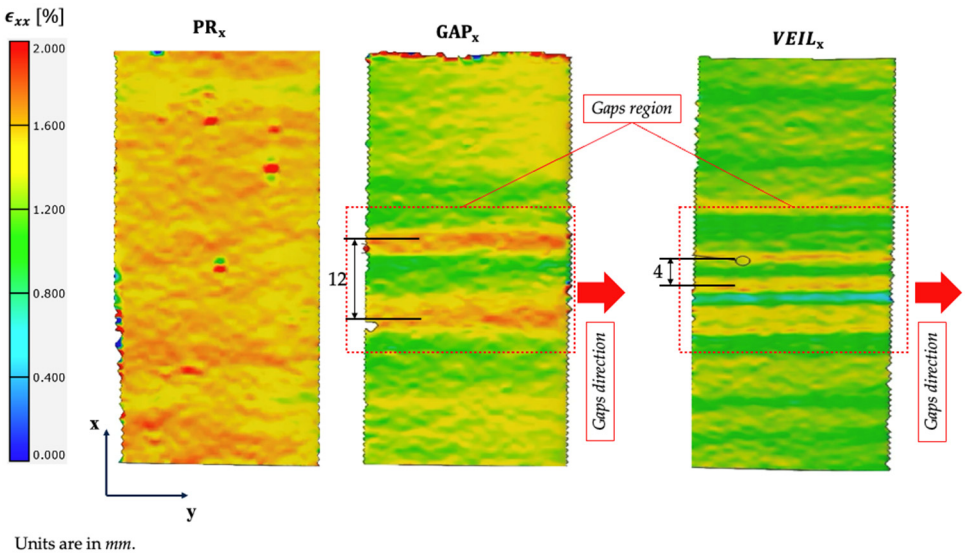

Figure 15. Strain distribution maps from DIC analysis for samples loaded in x-direction at failure.

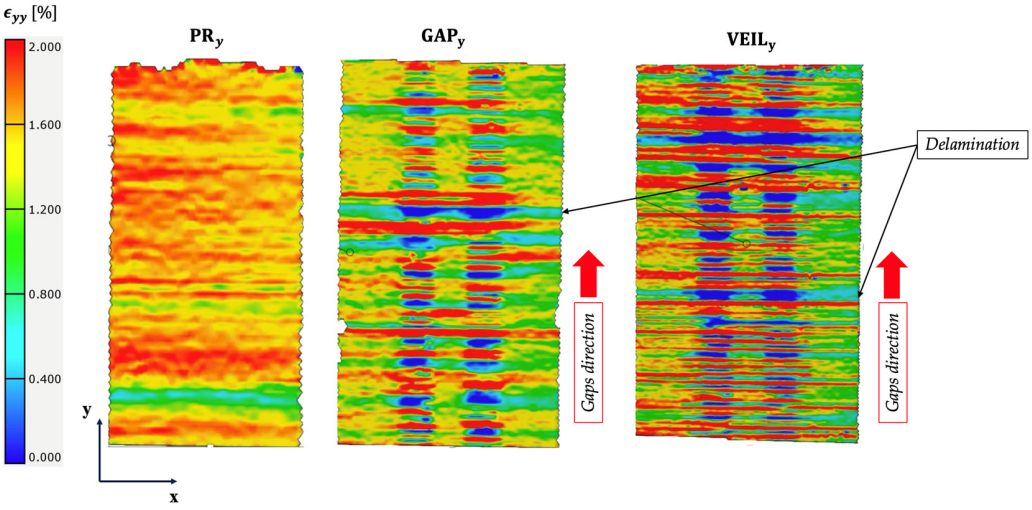

Figure 16. Strain distribution maps from DIC analysis for samples loaded in y-direction at failure.

Figure 16 shows ε_{yy} maps under y-direction loading for PR_y, GAP_y, and $VEIL_y$. In PR_y, ε_{yy} strain distribution exhibited relatively uniform spacing for horizontal strain streaks. This behavior is attributed to transverse matrix cracking, which is likely to initiate near the free edge and propagate across the sample width. This behavior is driven by shear-lag effects, where load transfer among transverse plies governs continued matrix cracking until saturation with the transverse cracks, after which the efficiency of the primary load-bearing plies diminishes, and ultimate failure occurred.

The characteristic strain distribution in the center of GAP_y represents the removed 90° tow, which is now oriented in the direction of the applied loading. Ply waviness represents the original 0° layers, which are, however, not load bearing in the y-direction. The GAP_y sample exhibited sharp alternating bands of high ~2.0 % strain (represented by red color) and relief down to ~0.0–0.1 % (blue color) in between those streaks. The average spacing in the x-direction between narrow streaks was measured to be 3.2 mm (using center-to-center lines), while the width of the band in the x-direction measured 19.05 mm and it indicated the interaction of the missing tow with the progression of the transverse matrix cracking observed in the PR_y sample. The observed strain distribution behavior in pristine and GAP_y samples is further investigated in the following section using PFA results.

$VEIL_y$ preserved the alternating red/blue banding with significantly increased intensity in the contrast and reduced average spacing between the strain streaks in the y-direction, which measured 2.4 mm. The dark blue color in both $VEIL_y$ and GAP_y represents delamination zones. Veiled samples showed an average delamination size of 20 mm^2 versus 10 mm^2 in GAP_y. The fundamental failure modes remain unchanged and reduced out-of-plane waviness in the non-primary plies leads to a denser network of transverse cracks and more extensive, yet stable, delamination. These differences confirm that incorporating a veil alters damage propagation by promoting greater levels of damage saturation prior to failure, both in terms of the delamination and transverse cracking.

4.6. Analysis of Damage Modes from PFA Results

To gain further insight into the damage progression, especially around the resin-rich regions, progressive failure analysis of pristine and GAP samples was performed. To represent the complex non-uniform cure morphology of the GAP samples, the structural simulations used the geometry from compaction simulations as discussed in Section 3.

Figure 17a presents the longitudinal strain distribution (ε_{xx}) at failure for the PR_x sample, comparing experimental measurements with FEA predictions. The experimental strain map shows a relatively uniform field with localized peaks exceeding 2%, likely due to material heterogeneities or experimental noise. The FEA results exhibit a similar uniform strain distribution, with values centered around 0.0141 ± 0.00037, capturing the overall deformation trend observed in the experiment (Figure 17a). The matrix damage profile along section A-A indicates that failure initiates in the tensile-loaded region, with early failure of the 90° plies transferring the load to the adjacent 0° plies. Notably, no cohesive damage was observed in the pristine samples under x-direction loading, highlighting the dominant role of matrix cracking in the failure mechanism (Figure 17b).

Figure 18 illustrates the strain and matrix damage distributions at failure for the GAP_x sample, where the presence of staggered fiber tow-gaps significantly alters the failure behavior. The experimental ε_{xx} map reveals strong localization of tensile and strain relief, forming alternating horizontal bands that align with the position of the gap. This non-uniform deformation is captured by the FEA, which predicts concentrated strain fields near the gap boundaries, with values reaching up to ~0.0114. Compared to the pristine sample, the GAP_x laminate exhibits greater anisotropy in the strain field, reflecting the influence of

the tow-gaps on stress redistribution and load transfer. The corresponding matrix damage plot shows that damage initiates and propagates near the tow-gap region, both in-plane and through-thickness. The section A-A profile confirms this behavior, showing localized matrix failure zones that penetrate the laminate and shift load paths into adjacent plies. These damage zones appear near the edges of the gap, where strain concentrations are highest.

Figure 19 provides insight into how different tow-gap ply configurations (Figure 19a–e) influence cohesive-zone damage and delamination behavior at failure for the GAP_x sample. The simulations reveal that the location and stacking sequence of the gap significantly affect both the initiation and propagation of interlaminar damage. Figure 19a,b, which shows Gap 1 at the interface between the top plies, exhibits early and extensive delamination propagating from the resin-rich region toward the free edge. The localized fully damaged cohesive elements confirm that this region acted as delamination initiation sites. As the tow-gap shifts toward midplane plies, as in Gap 5 in Figure 19c, the cohesive damage becomes confined and less severe. Furthermore, Gaps 7 and 8, shown in Figure 19d,e, show multiple delamination fronts forming near the resin-rich region, specifically, around the free edge near the bottom laminate surface. This indicates complex interactions between fiber orientation, local stiffness mismatch, and stress redistribution near the gap. Overall, these cohesive damage maps demonstrate that delamination is the most pronounced when the tow-gap induced resin-rich pocket appears closer to the laminate outer surface. This trend highlights the strong correlation between the depth of the resin-rich regions and its impact on through-thickness damage evolution. These combined PFA and DIC results indicate that the presence of the veil is primarily seen in the reduced fiber waviness that plays a role in preventing extensive delamination from forming, particularly in the GAP_x samples.

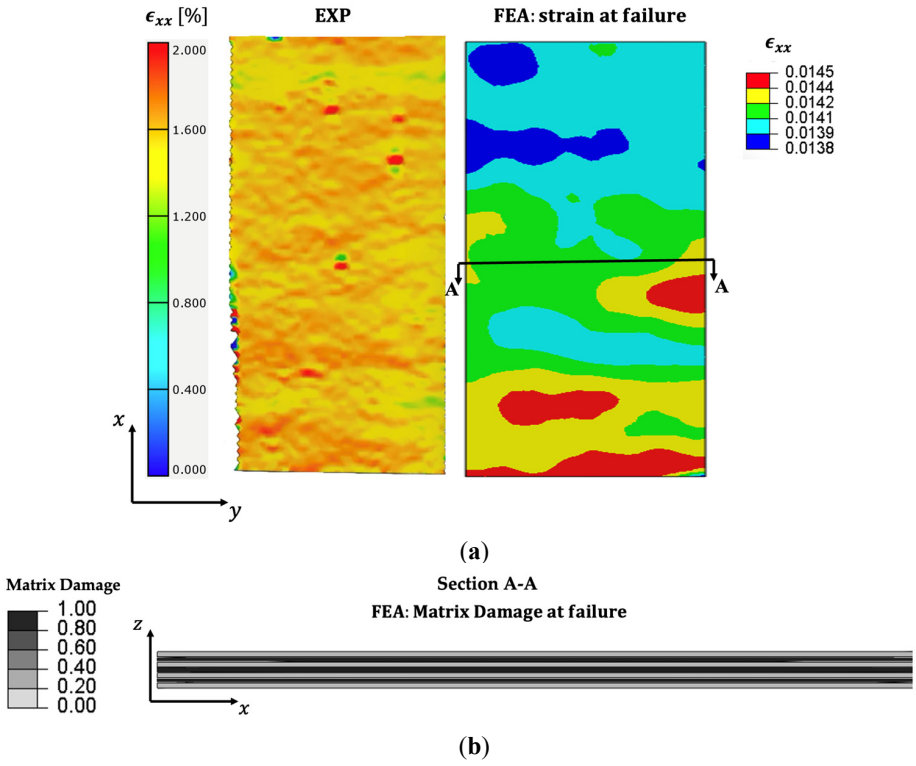

Figure 17. (**a**) Strain distributions at failure from experiment and simulation; (**b**) corresponding matrix damage along section A-A for PR_x sample.

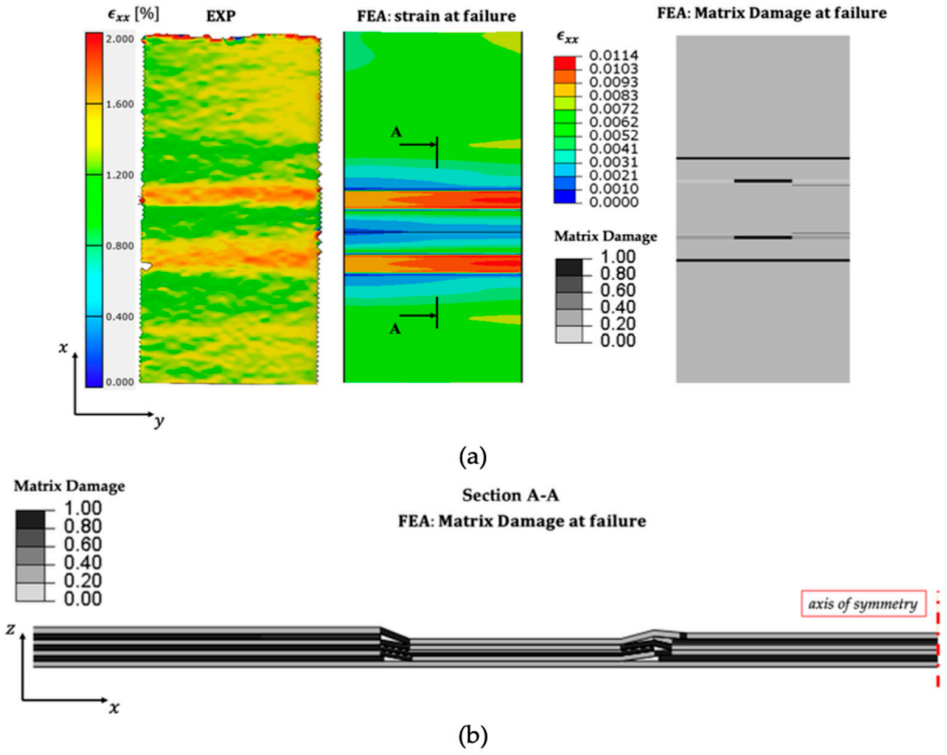

Figure 18. (**a**) Strain distributions at failure from experiment and simulation; (**b**) corresponding matrix damage along section A-A for GAP_x sample.

Figure 20 contrasts the transverse response of the PR_y laminate, showing that strain localized in the 90° plies and that matrix cracking initiated at the free edges of those plies, progressively causing transverse cracking until only the 0° layers carried the load [35,36]. The agreement between the experimental strain field and the FEA predictions confirmed that failure is dominated by edge-driven cracking of the transverse plies. By comparison, the GAP_y specimen (Figure 21) revealed a different failure scenario: the tow-gaps created resin-rich regions that acted as stress risers, shifting the onset of matrix cracking from the free edges to the interior of the laminate. Transverse cracks nucleated at these resin-rich sites and then propagated outward through the ply interfaces, leading to a more localized delamination process. While delamination was evident in GAP_y, its extent was notably less severe than that observed in the GAP_x configuration, indicating that the orientation of the gap relative to the loading direction played a significant role in damage evolution.

It should be noted that the PFA modeling in this study was intended for a failure-mode analysis to reveal the mechanisms of gap-induced behavior. The PFA results for pristine configurations were within a 5–7% error of the experimental results for the modulus and the strength in x- and y-direction. For the pristine x-direction specimen (PR_x), the PFA predicted a maximum strength of about 1390 MPa compared to the experimental 1480 MPa, giving an error of roughly 6%. For the pristine y-direction specimen (PR_y), the PFA predicted about 1080 MPa versus the experimental 1150 MPa, an error of about 6%. For the longitudinal gap configuration (GAP_x), the experimental strength was about 1300 MPa while the PFA predicted 1100 MPa, corresponding to an error of roughly 15%. For the transverse gap (GAP_y), the experimental strength was about 730 MPa while the PFA predicted 500 MPa, yielding an error of roughly 32%. The higher error in the latter case is likely due to the greater sensitivity of the morphology and resin-rich pocket geometry in the tow-gap direction. Furthermore, since explicit modeling of veils in the interlaminar and inside-gap regions was not attempted, the PFA simulations were primarily used for understanding the effects of waviness on the failure modes in the samples with gaps.

Therefore, the objective for PFA was to capture how compaction-driven morphology, ply waviness, resin-rich regions, and local strain concentrations affect damage initiation and progression. Since the presence of veils was shown to reduce the detriment of the ply waviness and resin-rich regions on the apparent strength, the simulation results offer an insight into the driving mechanisms of the failure and the corresponding failure modes that develop as a result of the non-uniform morphology around the gap region.

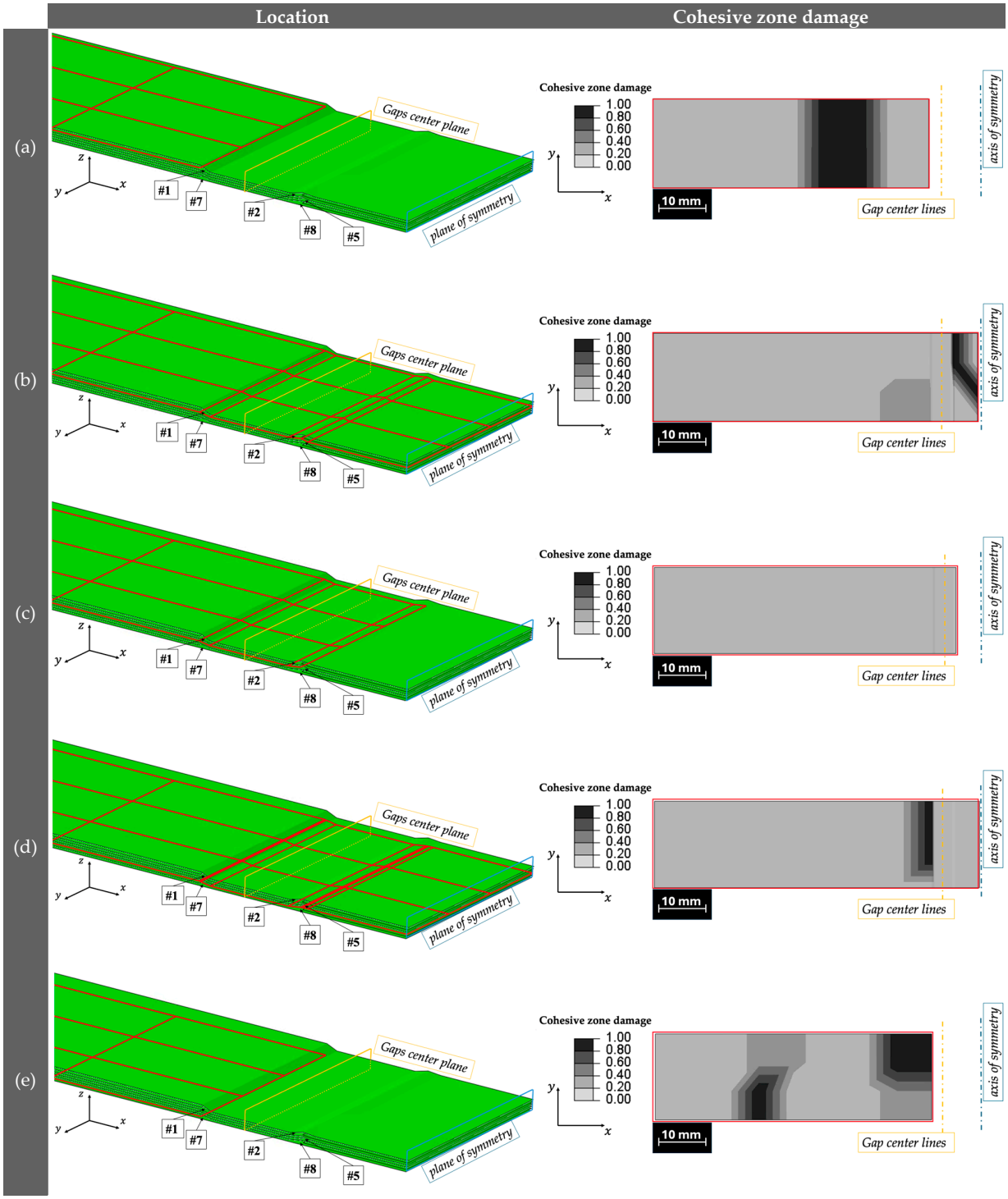

Figure 19. Tow-gap ply configurations in the laminate and their corresponding cohesive-zone damage contours at failure for the sample GAP_X. Each subfigure (**a**–**e**) illustrates the cohesive damage distribution within an individual ply of the laminate. The numbers indicate the resin-reach regions corresponding to the gap-closure side numbers shown in Figure 1.

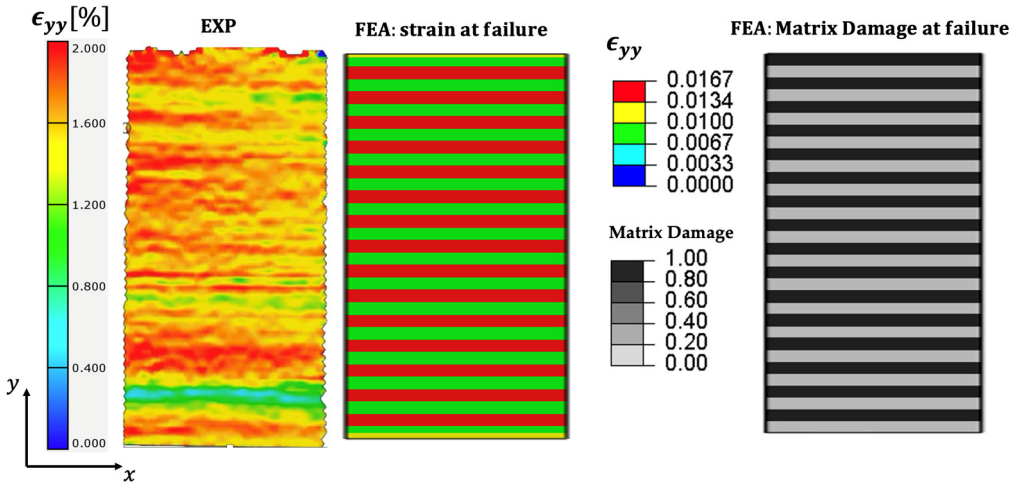

Figure 20. Strain distributions at failure from experiment and simulation, with corresponding matrix damage for PR_y sample.

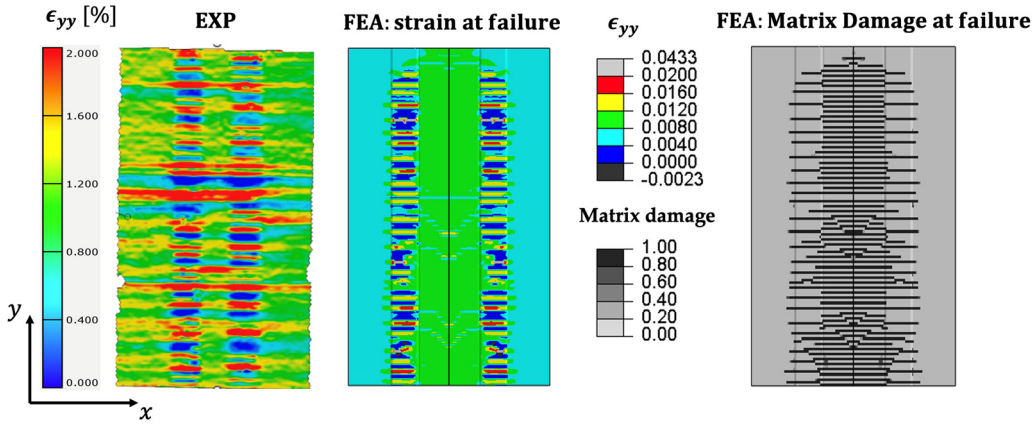

Figure 21. Strain distributions at failure from experiment and simulation and corresponding matrix damage for GAPy sample.

5. Conclusions

Introducing thin PEI veils into tow-gaps during AFP yielded marked improvements in both composite morphology and mechanical performance. The case of a cross-ply laminate with rectangular staggered tow-gaps was chosen as a benchmark configuration to provide insight into the formation of non-uniform morphology around the gap regions and to study the effect of veil placement on fundamental compaction and resin-flow mechanisms. The cross-ply laminates have a well-understood failure behavior that is sensitive to the density of transverse matrix cracking [5,6]. Therefore, this stacking sequence presented an appropriate laminate system to study how the changes in fiber waviness around the tow-gap region can affect both (i) changes in failure mode with tow gaps and (ii) changes in the failure signature with veils.

Surface profilometry showed that veils halved the peak-to-valley height variation, from approximately 0.47 mm in unreinforced gaps to 0.23 mm, while preventing ply sinking and smoothing out surface waviness. Optical microscopy and micro-CT confirmed that these veils reduced continuous resin channels, as well as resin-rich pockets from 250–400 μm to below 50 μm. This allowed the laminate to sustain straighter fiber paths through an interpenetrated fiber–veil network. Mechanically, these morphological gains translated into near-full recovery of tensile strength and stiffness under x-direction loading: strength rose from ~1300 MPa (GAP_x) to ~1476 MPa ($VEIL_x$), and stiffness increased from ~81 GPa to ~100 GPa, with DIC strain maps showing a one-third reduction in peak local

strains. In contrast, y-direction tests highlighted the veils' inability to substitute for the missing load bearing 90° fibers. Although surface waviness in non-primary 0° plies was still reduced, tensile strength remained below that of pristine laminates, underscoring the need for defect- and load-oriented reinforcement strategies in multidirectional layups.

Transverse cracking in the PR_y laminate initiated at the free edges of the 90° plies and advanced inward as neighboring layers accumulated damage. In the GAP configuration, the omission of a tow creates a material discontinuity that leads to stress concentration and damage. These fractures initially appear as narrow strain bands: as local waviness around the tow-gap amplifies, the matrix cracks evolve into broader, specimen-spanning streaks. Combining DIC and tensile strength results reveals that thermoplastic veils placed in the y-direction most effectively bolster strength by preventing ply sinking in the x-direction. In contrast, when y-aligned veils are tested in the y-direction, they alter damage propagation but do not produce a net strength increase. The PFA results indicated that damage inside the GAP sample developed around the resin-rich regions near the laminate surface. The PFA results revealed strong correlations between tow-gap depth, ply location, and failure initiation sites. This highlights the critical influence of manufacturing-induced geometry on load redistribution and ultimate damage progression.

The results indicate that morphology control and the scaffold effect of the thermoplastic veil are the primary drivers of strength recovery. In the x-direction, where 0° plies experience suppressed waviness, nearly complete strength restoration is observed, whereas in the y-direction, where the absence of 90° reinforcement governs the load path, no significant strength gain occurs despite potential interlaminar toughening. DIC strain maps further corroborate this interpretation, showing that the reduction in strain hot spots coincides with the measured decrease in ply waviness, underscoring a geometry-dominated strengthening mechanism. It is noted that the strength recovery was observed primarily when the veil suppressed waviness in the load-bearing plies (x-direction). This load-path dependence reflects the intended role of the veil as a morphology-conditioning scaffold rather than a substitute for missing fibers. In multiaxial laminates, the same principle can be applied by selectively placing veils in or adjacent to gaps that intersect critical load paths, so the approach remains viable for complex AFP structures while also reducing variability and stabilizing damage evolution even when net strength is not increased.

Taken together, these findings establish that selective placement of thermoplastic veils in tow-gaps is an effective strategy for mitigating out-of-plane fiber waviness and resin-rich defects, and associated strength knockdown, especially when preventing waviness in the load-bearing plies. Embedding compaction and failure simulations into the design workflow provides a powerful toolset for enabling weight-efficient, high-performance AFP laminates with predictable mechanical behavior.

While this study provides insights into mitigating waviness and resin-rich regions with thermoplastic veils, certain limitations should be acknowledged. The laminates were produced using manual layup with roller compaction, which does not capture all aspects of AFP deposition such as steering effects and thermal history. The numerical model employed idealized gap geometries. As the presented veils were generally designed for compatibility with the resin in terms of the wetting and bonding, future work will focus on validating the benchmark framework by exploring a wider range of veil materials and architectures, examining different gap geometries and processing conditions, and quantifying potential trade-offs such as added mass and resin-flow modifications. Future work will also extend this benchmark framework to include damage-tolerance evaluations such as compression-after-impact, open-hole tension/compression, and fatigue testing, which are particularly sensitive to fiber waviness and resin-rich regions. Variability is illustrated with box-and-whisker plots, and more comprehensive statistical analyses such

as ANOVA will be incorporated in future studies to further substantiate these comparisons. Industrial scalability, including potential AFP–head integration and associated production impacts, will also be assessed.

Author Contributions: Conceptualization, O.G.K. and A.R.; methodology, A.R.; software, A.R.; validation, A.R.; formal analysis, A.R., K.C. and S.G.K.; investigation, A.R.; resources, O.G.K.; data curation, A.R.; writing—original draft preparation, A.R., K.C. and S.G.K.; writing—review and editing, O.G.K.; visualization, A.R.; supervision, O.G.K.; project administration, O.G.K. and A.R.; funding acquisition, O.G.K.; All authors have read and agreed to the published version of the manuscript.

Funding: This research was supported by the Air Force Office of Scientific Research (AFOSR) under award FA9550-25-1-0004. A.R. and O.G.K. acknowledge this support.

Data Availability Statement: The data presented in this study are available on request from the corresponding author.

Acknowledgments: The authors gratefully acknowledge Technical Fibre Products Ltd. (TFP) for generously providing the polyetherimide thermoplastic veils (T2744-05 and T2744-06) used in this research. We also thank Rigaku Corporation, and in particular Ted Huang, for their invaluable assistance with high-resolution micro-computed tomography scanning and fiber analysis.

Conflicts of Interest: The authors declare no conflict of interest.

Appendix A

Table A1. Properties of IM7/8552 [37].

Property	Value	Unit
Longitudinal Young's modulus	147,000	(MPa)
Transverse Young's modulus	8700	(MPa)
In-plane shear modulus	5200	(MPa)
Major Poisson ratio	0.32	
Minor Poisson ratio	0.45	
Transverse tensile strength	80	(MPa)
Shear strength	98	(MPa)
Mode I fracture toughness	0.24	(kJ/m^2)
Mode II fracture toughness	0.74	(kJ/m^2)
BK exponent for mode-mixity	2.1	
Transverse compressive strength	288	(MPa)
Fracture plane angle for pure transverse compression	0.925	(rad)
3-direction Young's modulus	8700	(MPa)
Shear modulus in 1–3 plane	5200	(MPa)
Shear modulus in 1–2 plane	3000	(MPa)
Poisson's ratio in 2–3 plane	0.32	
Longitudinal tensile strength	2600	(MPa)
Longitudinal tensile strength ratio	0.375	
Longitudinal tensile fracture toughness	35.90	(kJ/m^2)
Longitudinal tensile fracture toughness ratio	0.75	

Table A1. *Cont.*

Property	Value	Unit
Longitudinal compressive strength	1700	(MPa)
Longitudinal compressive strength ratio	0.375	
Longitudinal compressive fracture toughness	10.68	(kJ/m^2)
Longitudinal fracture toughness ratio	0.75	

Table A2. Cohesive properties of IM7/8552 [37].

Property	Value	Unit
Mode I strength σ_I	80	(MPa)
Mode II strength σ_{II}	98	(MPa)
Normal mode fracture energy G_{Ic}	0.24	(kJ/m^2)
Shear mode fracture energy G_{II}	0.74	(kJ/m^2)
B-K exponent η	2.1	

References

1. Lukaszewicz, D.H.-J.A.; Ward, C.; Potter, K.D. The Engineering Aspects of Automated Prepreg Layup: History, Present and Future. *Compos. Part B Eng.* **2012**, *43*, 997–1009. [CrossRef]
2. Yan, L.; Chen, Z.C.; Shi, Y.; Mo, R. An Accurate Approach to Roller Path Generation for Robotic Fibre Placement of Free-form Surface Composites. *Robot. Comput.-Integr. Manuf.* **2014**, *30*, 277–286. [CrossRef]
3. Heinecke, F.; Willberg, C. Manufacturing-Induced Imperfections in Composite Parts Manufactured via Automated Fiber Placement. *J. Compos. Sci.* **2019**, *3*, 56. [CrossRef]
4. Brasington, A.; Sacco, C.; Halbritter, J.; Wehbe, R.; Harik, R. Automated Fiber Placement: A Review of History, Current Technologies, and Future Paths Forward. *Compos. Part C Open Access* **2021**, *6*, 100182. [CrossRef]
5. Fayazbakhsh, K.; Arian Nik, M.; Pasini, D.; Lessard, L. Defect Layer Method to Capture Effect of Gaps and Overlaps in Variable Stiffness Laminates Made by Automated Fiber Placement. *Compos. Struct.* **2013**, *97*, 245–251. [CrossRef]
6. Lan, M.; Cartié, D.; Davies, P.; Baley, C. Influence of Embedded Gap and Overlap Fiber Placement Defects on the Microstructure and Shear and Compression Properties of Carbon–Epoxy Laminates. *Compos. Part A Appl. Sci. Manuf.* **2016**, *82*, 198–207. [CrossRef]
7. Harik, R.; Saidy, C.; Williams, S.J.; Gurdal, Z.; Grimsley, B. Automated Fiber Placement Defect Identity Cards: Cause, Anticipation, Existence, Significance, and Progression. In Proceedings of the SAMPE 2018, Long Beach, CA, USA, 21–24 May 2018.
8. Wilhelmsson, D.; Gutkin, R.; Edgren, F.; Asp, L.E. An Experimental Study of Fibre Waviness and Its Effects on Compressive Properties of Unidirectional NCF Composites. *Compos. Part A Appl. Sci. Manuf.* **2018**, *107*, 665–674. [CrossRef]
9. Kulkarni, P.; Mali, K.D.; Singh, S. An Overview of the Formation of Fibre Waviness and Its Effect on the Mechanical Performance of Fibre Reinforced Polymer Composites. *Compos. Part A Appl. Sci. Manuf.* **2020**, *137*, 106013. [CrossRef]
10. Chai, E.Y.H.; Wang, W.C.; Christian, W.J.R. Experimental Study on the Effect of Waviness Defects on Composite Material Impact Dynamics. *Compos. Part B Eng.* **2024**, *283*, 111638. [CrossRef]
11. Jamora, V.C.; Rauch, V.; Kravchenko, S.G.; Kravchenko, O.G. Effect of Resin Bleed Out on Compaction Behavior of the Fiber Tow-gap Region during Automated Fiber Placement Manufacturing. *Polymers* **2023**, *16*, 31. [CrossRef]
12. Jamora, V.C.C.; Kravchenko, O.; Kravchenko, S. Process Modeling of a Multidirectional Laminate with Multiple Embedded Staggered Tow-gaps. In Proceedings of the AIAA SCITECH 2023 Forum, National Harbor, MD, USA, 23–27 January 2023; American Institute of Aeronautics and Astronautics: National Harbor, MD, USA, 2023.
13. Trochez, A.; Jamora, V.C.; Larson, R.; Wu, K.C.; Ghosh, D.; Kravchenko, O.G. Effects of Automated Fiber Placement Defects on High Strain Rate Compressive Response in Advanced Thermosetting Composites. *J. Compos. Mater.* **2021**, *55*, 4549–4562. [CrossRef]
14. Ghayoor, H.; Marsden, C.C.; Hoa, S.V.; Melro, A.R. Numerical Analysis of Resin-Rich Areas and Their Effects on Failure Initiation of Composites. *Compos. Part A Appl. Sci. Manuf.* **2019**, *117*, 125–133. [CrossRef]
15. Mahmood, A.S.; Summerscales, J.; James, M.N. Resin-Rich Volumes (RRV) and the Performance of Fibre-Reinforced Composites: A Review. *J. Compos. Sci.* **2022**, *6*, 53. [CrossRef]
16. Ahmadian, H.; Yang, M.; Soghrati, S. Effect of Resin-Rich Zones on the Failure Response of Carbon Fiber Reinforced Polymers. *Int. J. Solids Struct.* **2020**, *188–189*, 74–87. [CrossRef]

17. Del Rossi, D.; Cadran, V.; Thakur, P.; Palardy-Sim, M.; Lapalme, M.; Lessard, L. Experimental Investigation of the Effect of Half Gap/Half Overlap Defects on the Strength of Composite Structures Fabricated Using Automated Fibre Placement (AFP). *Compos. Part A Appl. Sci. Manuf.* **2021**, *150*, 106610. [CrossRef]
18. Marouene, A.; Legay, P.; Boukhili, R. Experimental and Numerical Investigation on the Open-Hole Compressive Strength of AFP Composites Containing Gaps and Overlaps. *J. Compos. Mater.* **2017**, *51*, 3631–3646. [CrossRef]
19. Maragoni, L.; Modenato, G.; De Rossi, N.; Vescovi, L.; Quaresimin, M. Effect of Fibre Waviness on the Compressive Fatigue Behavior of Woven Carbon/Epoxy Laminates. *Compos. Part B Eng.* **2020**, *199*, 108282. [CrossRef]
20. Sitohang, R.D.R.; Grouve, W.J.B.; Warnet, L.L.; Wijskamp, S.; Akkerman, R. The Relation between in-Plane Fiber Waviness Severity and First Ply Failure in Thermoplastic Composite Laminates. *Compos. Struct.* **2022**, *289*, 115374. [CrossRef]
21. Sitohang, R.D.R.; Grouve, W.J.B.; Warnet, L.L.; Akkerman, R. Effect of in-Plane Fiber Waviness Defects on the Compressive Properties of Quasi-Isotropic Thermoplastic Composites. *Compos. Struct.* **2021**, *272*, 114166. [CrossRef]
22. Altmann, A.; Gesell, P.; Drechsler, K. Strength Prediction of Ply Waviness in Composite Materials Considering Matrix Dominated Effects. *Compos. Struct.* **2015**, *127*, 51–59. [CrossRef]
23. Wang, J.; Potter, K.D.; Etches, J. Experimental Investigation and Characterisation Techniques of Compressive Fatigue Failure of Composites with Fibre Waviness at Ply Drops. *Compos. Struct.* **2013**, *100*, 398–403. [CrossRef]
24. Wang, S.; Akbolat, M.Ç.; Katnam, K.B.; Zou, Z.; Potluri, P.; Taylor, J. On the Interlaminar Fracture Behavior of Carbon/Epoxy Laminates Interleaved with Fiber-Hybrid Non-Woven Veils. *Polym. Compos.* **2024**, *45*, 3315–3326. [CrossRef]
25. Kuwata, M.; Hogg, P.J. Interlaminar Toughness of Interleaved CFRP Using Non-Woven Veils: Part 1. Mode-I Testing. *Compos. Part A Appl. Sci. Manuf.* **2011**, *42*, 1551–1559. [CrossRef]
26. Kuwata, M.; Hogg, P.J. Interlaminar Toughness of Interleaved CFRP Using Non-Woven Veils: Part 2. Mode-II Testing. *Compos. Part A Appl. Sci. Manuf.* **2011**, *42*, 1560–1570. [CrossRef]
27. Quan, D.; Bologna, F.; Scarselli, G.; Ivankovic, A.; Murphy, N. Interlaminar Fracture Toughness of Aerospace-Grade Carbon Fibre Reinforced Plastics Interleaved with Thermoplastic Veils. *Compos. Part A Appl. Sci. Manuf.* **2020**, *128*, 105642. [CrossRef]
28. Rautmann, M.; Gabriel, E.R.; Kim, B.C. Advanced Continuous Tow Shearing Process Utilising in-Line Tow Width Control in Fibre Steering. *Compos. Part A Appl. Sci. Manuf.* **2025**, *196*, 109025. [CrossRef]
29. Jacobsen, G. Mechanical Characterization of Stretch Broken Carbon Fiber Materials—IM7 Fiber in 8552 Resin. In Proceedings of the SAMPE'10 Spring Symposium Technical Conference Proceedings, Salt Lake City, UT, USA, 17–20 May 2010.
30. Hexcel. *HexPly® 8552 Product Data Sheet*; Hexcel Composites: Cambridge, UK; Hexcel Corporation: Stamford, CT, USA, 2013.
31. Bergan, A.C. New Developments in the CompDam Fiber Kinking Model for the Interaction of Kinking and Splitting Cracks with Application to Open Hole Compression Specimens. In Proceedings of the AIAA Scitech 2021 Forum, Nashville, TN, USA, 1–15 January 2021.
32. Leone, F.A.; Bergan, A.C.; Dávila, C.G. CompDam—Deformation Gradient Decomposition (DGD), v2.5.0 [Software]. NASA. 2019. Available online: https://github.com/nasa/CompDam_DGD (accessed on 10 August 2025).
33. Leone, F.A., Jr. Deformation Gradient Tensor Decomposition for Representing Matrix Cracks in Fiber-Reinforced Materials. *Compos. Part A Appl. Sci. Manuf.* **2015**, *76*, 334–341. [CrossRef]
34. Kassapoglou, C. *Design and Analysis of Composite Structures: With Applications to Aerospace Structures*; Wiley: Hoboken, NJ, USA, 2010.
35. Gyekenyesi, A.L. *Crack Development in Cross-Ply Laminates Under Uniaxial Tension; NASA Contractor Report 195464*; Prepared for NASA Lewis Research Center under Grant NAG3-1543, January; Cleveland State University: Cleveland, OH, USA, 1996.
36. Nairn, J.A. Matrix Microcracking in Composites. In *Comprehensive Composite Materials*; Kelly, A., Zweben, C., Eds.; Elsevier: Amsterdam, The Netherlands, 2000.
37. Larson, R.; Bergan, A.; Leone, F.; Kravchenko, O.G. Influence of Stochastic Adhesive Porosity and Material Variability on Failure Behavior of Adhesively Bonded Composite Sandwich Joints. *Compos. Struct.* **2023**, *306*, 116608. [CrossRef]

Disclaimer/Publisher's Note: The statements, opinions and data contained in all publications are solely those of the individual author(s) and contributor(s) and not of MDPI and/or the editor(s). MDPI and/or the editor(s) disclaim responsibility for any injury to people or property resulting from any ideas, methods, instructions or products referred to in the content.